# Liquid, Liquid Crystal, and Crystal States of Different Shaped Colloids in Nonuniform Fields via Osmotic Force Balance

*Lechuan Zhang, Alec J. Pellicciotti, Michelle Sandag, Michael A. Bevan**
Chemical & Biomolecular Engineering, Johns Hopkins University, Baltimore, MD, 21218, USA

## Abstract

We report a model to predict equilibrium density profiles for different shaped colloids in two-dimensional liquid, nematic, and crystal states in nonuniform external fields. The model predictions are validated against Monte Carlo simulations and optical microscopy experiments for circular, square, elliptical, and rectangular colloidal particles in AC electric fields between parallel electrodes. The model to predict the densities of all states of different shaped particles is based on a balance of the local quasi-2D osmotic pressure against a compressive force due to induced dipole-field interactions. The osmotic force balance (OFB) employs equations of state for hard ellipse liquid, nematic, and crystal state osmotic pressures, which are extended to additional particle shapes. The resulting simple analytical model is shown to accurately predict particle densities within liquid, liquid crystal, and crystal states for a broad range of particle shapes, system sizes, and field conditions. These findings provide a basis for quantitative design and control of fields to assemble and reconfigure colloidal particles in interfacial materials and devices.

keywords: superelliptical prisms | density profiles | AC electric fields | dipole-field potentials | equations of state

## Introduction

Understanding how to obtain different colloidal microstructural states assembled from any particle shape could enable numerous emerging particle based technologies. More specifically, the ability to predict how external fields and particle properties together can be designed to achieve target ordered states provides a basis to design, control, and optimize colloidal materials and devices. Although particle shape libraries with systematic variations have been related to free energy minimum crystal and liquid crystal states in computer simulations in 3D[1] and 2D[2] homogeneous systems, there has been limited progress in modeling or experiments to determine how to achieve such states in finite, bounded, inhomogeneous systems. Substrates and boundaries are common as supports and containers for colloidal materials, and fields (*e.g.*, gravity, shear, electric, etc.) are inherently part of processing and often unavoidable. Ultimately, being able to predict what colloidal microstructures assemble in a given field, including nonuniform fields, and for different particle shapes, is a necessary step for designing colloidal materials, processes, and devices in practical applications.

The role of gravity in producing density profiles in sedimentation equilibrium of colloidal dispersions has been known since Perrin,[3] which has been confirmed many times over, including coexistence between liquid and crystal states, and to high precision using advanced methods.[4] Sedimentation equilibrium of nonspherical colloidal clay platelets has been observed with coexistence of liquid, liquid crystal, and crystal states,[5] and in increasingly complex mixtures of multiple particle shapes.[6] The density profiles and phase transitions in sedimentation equilibrium are determined by a balance of local osmotic pressure changes and the force on particles due to

*To whom correspondence should be addressed. email: mabevan@jhu.edu

gravity. Osmotic pressure is well defined for thermodynamically large systems sizes, which is easily satisfied for macroscopic test tube scale experiments, but its application on microscopic scales is less obvious. However, prior work has validated multistate sedimentation equilibrium profiles for density variations approaching particle dimensions,[7] and shown other modeling approaches are needed for density variations comparable to, or smaller than, particle dimensions (*i.e.*, classical density functional theory[8-9]). Practically, multistate equilibria of spherical, plate, and rod shaped colloidal particles in linear gravitational potentials is relatively well understood, including experiments and simulations for different particle shapes, interactions, and mixtures.[9-10]

It is important to understand equilibrium colloidal phase behavior and assembly in other fields other than gravity (*e.g.*, electric, magnetic, optical). Although colloidal transport in external fields is studied extensively (*e.g.*, sedimentation, electrophoresis, dielectrophoresis, etc.[11-14]), equilibrium density profiles and microstructural states of colloids in different field types has received less attention. For example, colloidal assembly in nonuniform electric fields has been shown in experiments for spheres,[15-16] ellipsoids,[17-18] rods,[19-20] rectangular prisms,[21] clay platelets,[22] and a variety of other shapes,[23-25] but many studies do not consider spatial variations due to field nonuniformity. Concentrating density-matched spherical colloids in nonuniform AC electric fields via dipole-field interactions is one of few examples of bulk three dimensional systems modelled by an osmotic force balance.[26-28] Quasi-2D spherical colloidal density profiles in nonuniform AC electric fields have been investigated in experiments, simulations, and osmotic force balance models for spheres in radial harmonic wells,[29] multipolar field shapes,[30] and 2D crystals buckled into 3D morphologies (mediated by electric fields and gravity).[31] A recent simulation study investigated 2D hard ellipses in nonuniform fields with multi-state coexistence of inhomogeneous liquid, nematic, and crystal states,[32] which employed an osmotic force balance based on hard ellipse equations of state. Although other particles, fields, and configurations have been modelled via osmotic force balances (e.g., laser laser-induced freezing[33]), general models have not been reported for arbitrary particle shapes and nonuniform fields, particularly with experimental validation.

One limitation to predicting colloidal density profiles and states in external fields is a lack of equations of state for particles with different shapes and pair potentials. For example, equations of state have been developed for 3D hard sphere liquid[34] and crystal[35] states and more recently hard polyhedra liquid states.[36] 2D equations of state have been reported for liquid states of hard disks,[37] ellipses,[38-41] and general convex shapes,[42] as well as hard ellipse nematic states.[38-41] However, equations of state are generally unavailable for liquid, liquid crystal, and crystal states of different particle shapes, and particles with pair potentials other than hard interactions. While sedimentation equilibrium experiments have tested equations of state for hard spheres,[43-44] and some studies have employed osmotic balances to probe phase behavior and equations of state in novel colloidal (e.g., Janus,[45] active particles[46]) and molecular systems,[47-48] in general osmotic forces balances have not been used to develop new equations of state. As a result, to understand colloidal density profiles and states in nonuniform fields for different shaped particles with different potentials, it is also necessary to develop new equations of state to enable predictions based on osmotic force balances and related models.

In this work, we develop an osmotic force balance model that captures quasi-2D density profiles and microstructural states of disk, ellipse, square, and rectangular colloidal particles in nonuniform AC electric fields (**Fig. 1**). We first develop the osmotic force balance (OFB) model for elliptical prism particles, which is based on recently reported directly measured dipole-field

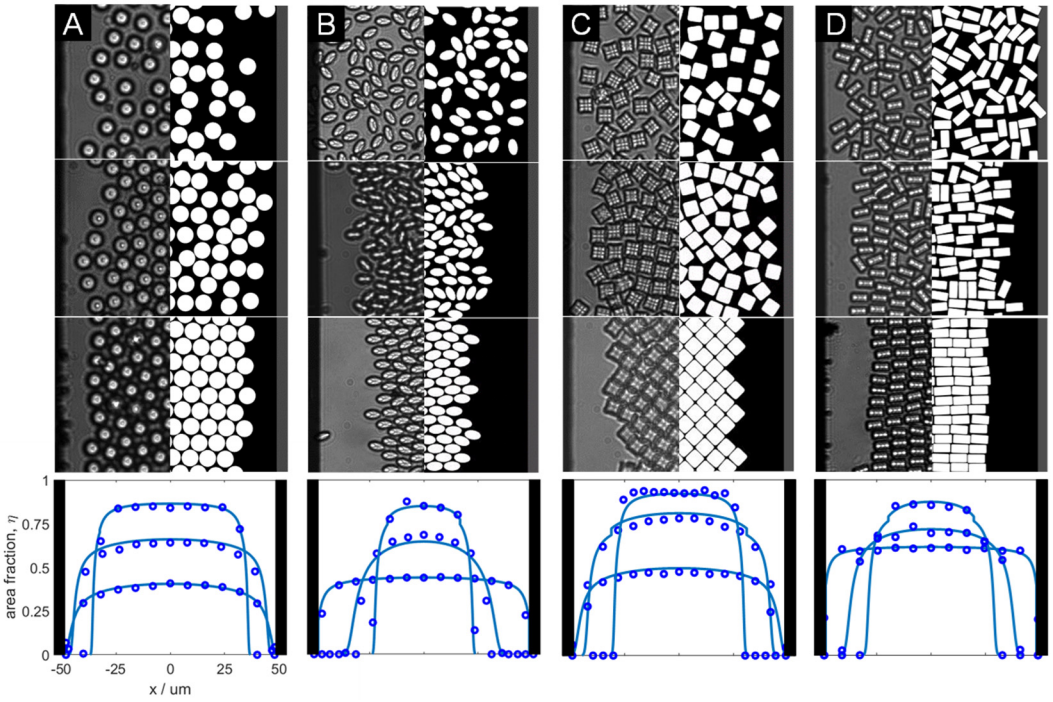


**Fig. 1. Overview of quasi-2D assembly of circular, elliptical, square, and rectangular prism colloids in nonuniform AC electric fields.** The field frequency is 5MHz and increasing voltage compresses particles at the electric field minimum in the center between coplanar parallel electrodes (to left and right sides of each image) via dipole-field interactions. Columns show optical microscopy images, Monte Carlo (MC) computer simulations renderings, and density profiles from microscopy, simulation, and a theoretical model for (A) disks, (B) ellipses, (C) squares, and (D) rectangles. Top three rows show increasing densities for liquids, dense liquid/liquid crystal, and crystal states. Bottom row shows density profiles (area fraction) from (points) MC simulations and (lines) an osmotic force balance expression developed in this work. The electrode gap, d=100 μm, provides an internal scale bars for each image.

interactions[49-50] as well as recently reported equations of state for liquid, nematic, and crystal states of 2D elliptical particles.[32] The OFB model is tested against Monte Carlo (MC) simulations for different particle sizes and concentrations and field parameters and then validated against optical microscopy experiments. We explore extensions of the model to different particle shapes to systematically vary aspect ratio (disks, ellipses) and introduce corners (squares, rectangles) that determine the number, types, and symmetry of assembled states.[2, 21, 51] We finally investigate modifying ellipse equations of state for liquid, nematic, and crystal states to enable osmotic force balance predictions of results for MC simulations and microscopy experiments on different particle shapes in nonuniform AC electric fields. The overall approach is designed to predict field conditions that produce assembled particle densities and corresponding liquid, liquid crystal, and crystal states for a broad range of colloidal particle shapes.

## Theory

*Osmotic Force Balance*

We consider concentration profiles of different effective hard particle shapes in AC electric fields, where the profile and field depend only on the *x*-coordinate (**Fig. 1**). In the following, predictions of concentration profiles in nonuniform fields are based on the local density approximation,[32, 52] where the equilibrium condition is given by a balance of local osmotic pressure

difference and local forces (*i.e.*, gradient of potential energy landscape) on particles as,[7, 29-31]

$$\Pi(x)-\Pi(x+\Delta x)=-\frac{dU(x)}{dx}\rho(x)\Delta x \tag{1}$$

where $\Pi$ is osmotic pressure, $U(x)$ is a position-dependent energy landscape, and $\rho(x)$ is local particle number density. For infinitesimally small changes in position ($\Delta x \to 0$), Eq. (1) is,

$$\frac{\partial \Pi}{\partial x}=-\frac{dU\left(x\right)}{dx}\rho\left(x\right) \tag{2}$$

which substituting effective area fraction for hard particles, $\eta=\rho A_p$, based on the effective particle area, $A_p$, and then re-arranging gives,

$$\int_{\eta}^{\eta(x)}\frac{\partial \Pi\left(\eta\right)}{\partial \eta}\eta^{-1}d\eta=\int_{0}^{x}\frac{dU\left(x\right)}{dx}dx \tag{3}$$

which can be solved to obtain the concentration profile, $\eta(x)$, for a given $U(x)$. The total number of particles within the concentration profile is given by,

$$N=\left(h/A_p\right)\int\eta(x)dx \tag{4}$$

where $h$ is box height (*e.g.*, image or simulation dimension in **Fig. 1**), and the limits of integration correspond to where the density vanishes.

*Dipole-Field Potential Energy*

To solve the osmotic force balance, it is necessary to specify the potential energy landscape in lab coordinates on the right-hand-side of Eqs. (1)-(3). The dipole field potential energy has been directly measured and captured by a validated simple model for quasi-2D states of superelliptical prism particles in high-frequency nonuniform AC electric fields between coplanar electrodes (**Fig. 1**).[49] By neglecting the orientation-dependence of the dipole-field potential, the position-dependent dipole-field potential energy for input in Eqs. (1)-(3) is simplifies to,[49-50]

$$U^{df}\left(x\right)=-PE_z^2\left(x\right) \tag{5}$$

where the amplitude, $P=\varepsilon_m v_p f_{cm} f_\eta$, depends on the particle volume, $v_p$, and the particle and medium material properties via the Clausius–Mossotti factor, $f_{cm}$, given by,[50, 53]

$$f_{\mathrm{cm}}=\mathrm{Re}\left[\frac{\tilde{\varepsilon}_p-\tilde{\varepsilon}_m}{3\tilde{\varepsilon}_m+\left(\tilde{\varepsilon}_p-\tilde{\varepsilon}_m\right)}\right],\quad \tilde{\varepsilon}_m=\varepsilon_m-i\sigma_m/\omega,\quad \tilde{\varepsilon}_p=\varepsilon_p-i\sigma_p/\omega \tag{6}$$

where $\varepsilon_x$ and $\sigma_x$ are particle and medium dielectric constants and conductivities, and $\omega$ is AC field frequency. The term $f_\eta=1-[10^{-5}/\exp(10\eta)]$ accounts for a diminished field within dense crystalline domains as observed in past work on spherical[54] and anisotropic[55] particles (analogous with 3D electrorheological fluids[56] and crystals,[57] but different due to 3D field outside quasi-2D domains). The position dependence in Eq. (5) is given by the $x$-dependence of the $z$-component of the electric field, $E_z(x)$, given by an analytical solution,[58] and well approximated by,

$$E_z(x) = \frac{E_0}{\pi}\left[\frac{-756\left(|x|/d\right)^2 + 480\left(|x|/d\right)}{100\left(|x|/d\right) - 55}\right] \tag{7}$$

where $E_0 = (8^{-0.5})V_{pp}/d$, where the factor $(8^{-0.5})$ accounts for time-averaging a sinusoidal waveform, (in contrast, the factor is $(12^{-0.5})$ for a triangular waveform), $V_{pp}$ is peak-to-peak voltage (for AC fields with different waveforms), and $d$ is the electrode gap width. Eq. (7) is accurate to within <1% error over the entire position range.

*Hard Superellipse Equations of State*

With specification of the potential energy landscape on the right-hand-side of Eqs. (1)-(3) , to obtain density profiles, it is necessary on the left-hand-side of the same equations to relate $\Pi$ and $\rho$ via equations of state given by,

$$\Pi = kT\rho Z \tag{8}$$

where $k$ is Boltzmann's constant, $T$ is the absolute temperature, and $Z$ is the compressibility factor. Functional forms for compressibility factors for varying aspect ratio hard ellipses in liquid, nematic, and crystal states were recently reported obtained by modifying first-principle forms[39] to match computer simulations.[32, 40] These compressibility factors are reported here with adjustable parameters to enable their fit to hard superellipse particle data in this study. In brief, the fluid compressibility factor for hard disks is given in terms of area fraction, $\eta$, by,[37]

$$Z_{F,HD}(\eta) = \left(1 + \eta^2/8\right)\left(1-\eta\right)^2 \tag{9}$$

which can be incorporated into a semi-empirical model[39] for the hard ellipse fluid compressibility factor, $Z_F$, that was adapted to accurately capture hard ellipse simulated compressibility factor data[40] with a form given by,[32]

$$Z_F(\eta) = 1 + \alpha\left[-0.12\eta^{2.5}\left(s-1\right)^2 + 0.21\left(s-1\right) + 1\right]\left[Z_{F,HD}(\eta) - 1\right] \tag{10}$$

where $s=a_x/a_y$ is aspect ratio given by particle major and minor radii, $a_x$ and $a_y$, and $\alpha$=1 for disks and ellipses but is allowed as an adjustable parameter to fit hard superellipse data. The nematic compressibility factor, $Z_N$, based on a density functional theory study[38] includes corrections to the hard ellipse fluid equation of state to accurately capture reported compressibility factor data[40] as,

$$Z_N = Z_F(\eta) + \left[1.7\left(s-1.6\right)\left(\eta - \eta_N\right)^{1.6}\right]\left[Z_{F,HD}(\eta) - 1\right] \tag{11}$$

where $\eta_N$ is the fluid-nematic transition area fraction. To estimate a crystal equation of state, we consider forms from free volume theory for anisotropic particles,[59-60] and simple forms[44] for hard sphere crystals,[35] to arrive at a crystal state compressibility factor, $Z_C$, given by,

$$Z_C(\eta) = \beta/\left(\eta_{CP} - \eta\right) \tag{12}$$

where $\eta_{CP}$ is the shape-dependent close packed area fraction, $\beta=(\eta_{CP}-\eta_M)(\eta_F/\eta_M)Z_N(\eta_F)$ is a defined constant designed to ensure $\Pi_N=\Pi_C$ at melting and freezing in Eq. (8), and $\eta_M$ and $\eta_F$ are the crystal-nematic (melting) and nematic-crystal (freezing) transition area fractions. Each equation of state in Eqs. (9)-(12) is applicable for states between boundaries defined by aspect ratio dependent area fractions for the nematic, $\eta_N$, freezing, $\eta_F$, and melting, $\eta_M$, transitions given by,

$$\eta_N = 0.678 - 0.053s \;\; 1.6 \le s \le 2$$
$$\eta_{\mathrm{F}} = 0.626 + 0.074s, \;\; \eta_{\mathrm{M}} = 0.639 + 0.076s \;\; 1 \le s \le 2 \tag{13}$$

which approach infinite system size hard disk[2, 61] and hard ellipse[32, 40-41] values in the absence of fields and are validated for nematic states mediated by dipole field potentials in this study.

*Superelliptical Prisms*

Particle shapes investigated in this work are all superelliptical prisms, where the equation of their projected 2D perimeter is given by,

$$\left|x/a_x\right|^n + \left|y/a_y\right|^n = 1 \tag{14}$$

where $n$ determines particle corner shape. Superellipse shapes include (**Fig. 1**) disks ($n$=2, $s$=1), ellipses ($n$=2, $s$>1), squares ($n\to\infty$, $s$=1), and rectangles ($n\to\infty$, $s$>1). Superelliptical prism particle of thickness $2a_z$ have volumes, $v_{\mathrm{p}}$, and areas, $A_{\mathrm{p}}$, given by,

$$v_P = 2a_z A_P, \;\; A_p = 4a_{\mathrm{x}}a_{\mathrm{y}}\left[\Gamma\left(1+n^{-1}\right)\right]^2\left[\Gamma\left(1+2n^{-1}\right)\right]^{-1} \tag{15}$$

where $\Gamma$ is the gamma function. The superellipse particle area can be used to relate the number of particles per area, $\rho$, to quasi-2D area fractions, $\eta$, for use in equations of states (Eqs. (8)-(12)) as,

$$\eta = A_p\rho \tag{16}$$

which can be adjusted for particles with short-range interactions compared to particle dimensions,[62] by adding to $a_{\mathrm{x}}$ and $a_{\mathrm{y}}$ in Eq. (15), a constant, $\delta$, given by,[63]

$$\delta = (1/2)\int_0^\infty \left[1 - \exp\left(-U(r)/kT\right)\right]dr \tag{17}$$

where in this study we consider a repulsive pair potential between similar sized particles with electrostatic double layers given by,[12]

$$U^e(r) = Ba\exp(-\kappa r), \;\; B = 32\pi\varepsilon_m\left(\frac{kT}{e}\right)^2\tanh^2\left(\frac{e\psi}{4kT}\right) \tag{18}$$

where $r$ is surface separation, $e$ is elemental charge, $\psi$ is the colloid surface potential, and $\kappa$ is the inverse Debye length. This expression is simplified for unit valence electrolyte and valid for thin double layers compared to particle radius ($\kappa a$>>1).[12]

## Materials & Methods

*Monte Carlo Simulations.* Monte Carlo simulations of superelliptical prism particles were performed in the canonical (NVT) ensemble using the methods and potentials in our previous work.[53, 55] In brief, the energy, $u_i$, of each particle $i$ is,

$$u_i = u_i^{df}(x_i) + \sum_{j=1, i\neq j}^{N_b}\left[u_{ij}^{dd}\left(x_i, \theta_i, \theta_j, x_{ij}, y_{ij}\right) + u_{ij}^{hp}\left(x_i, \theta_i, \theta_j, x_{ij}, y_{ij}\right)\right] \tag{19}$$

where $x_i$, $y_i$, $\theta_i$ are each particle's lab position and orientation coordinates, and $x_{ij}$, $y_{ij}$, $\theta_{ij}$ are relative particle position and orientation coordinates. The dipole-field, $u^{df}$, potential is given in Eq. (5), and the exact functional form for the dipole-dipole, $u^{dd}$, potential for superelliptical prisms is described

in detail in our previous work.[55] Particles were constrained in 2D with periodic boundary conditions perpendicular to the electrodes. Particle geometry for the hard overlap condition[2] is given by the superellipse equation. Simulations were initialized from a stretched hexagonal lattice (disk and ellipse) or stretched square lattice (square and rectangle) centered at the electrode gap center. All simulations were equilibrated for 75000 steps when potential energy reached a plateau minimum. Other simulation parameters are summarized in **Tables 1**,**2**.

*Particle Fabrication*. Anisotropic superelliptical prism epoxy particles (all chemicals from MicroChem) were fabricated using photolithography with similar methods to prior studies.[21] In brief, Omnicoat and SU-8 2002 were spin coated at 3000 rpm on a silicon wafer followed by heat treatment. A particle shape photomask was used to pattern particles on a wafer with a UV exposure energy of 80 mJ/cm$^2$ and then heat-treated. Uncured excess SU-8 was removed by immersing in PG Developer and isopropyl alcohol. Particle dimensions were confirmed with a laser-scanning microscope (Keyence). Particles on wafers were treated with 50% sulfuric acid to yield negative surface charge and cleaned with deionized water. Particles are released by PG Remover and cleaned with isopropyl alcohol and deionized water. These steps yield maximum negative surface charge to prevent aggregations and irreversible deposition on electrodes.[21, 64]

*Microscopy and Particle Tracking.* The microscopy cell was similar to prior studies.[16, 50, 54-55] An O-ring (McMaster-Carr) was placed on microfabricated interdigitated gold electrodes patterned on a glass slide. Particles were dispersed and pipetted into the O-ring to give the target particle concentration. Electrodes were connected to a function generator (Agilent 33220A) to apply sinusoidal AC fields at various field amplitudes and 5MHz frequency. Particles were imaged with an inverted microscope (Zeiss) using a 40× objective. Videos were captured using a CCD camera (Hamamatsu, Orca-ER) and Streampix (Norpix) or MATLAB software. Particle centroid position ($x$,$y$) and long-axis orientation ($\theta$) were tracked using previously reported MATLAB algorithms.[50] Experimental density profiles were obtained from ~50~1000 images over 10 min after each sample equilibrated at a given field condition. Density profiles were binned according to particle long axis dimensions ($2a_x$). Central area fractions, $\eta_0$, were averaged over the three center bins with error bars based on the lowest and highest values observed during all sampling.

## Results & Discussion

*Approach Overview*

We systematically investigate how different shaped particles pack into states with different density profiles via induced dipolar interactions with nonuniform AC electric fields (Eq. (5)). Because the local density essentially determines whether states are liquid, liquid crystal, or crystal, the ability to predict density profiles determines the degree of positional and orientational order of particles within electric fields. Equations of state for 2D anisotropic particles have previously been investigated in simulation studies of homogeneous systems of ellipses[38-41] and more recently by our group in inhomogeneous systems.[32] As a result, we first investigate density profiles of effective hard ellipses in nonuniform AC electric fields as a function of parameters related to the particles (number, size, area fraction), field conditions (voltage, electrode gap), and simulation parameters (box size). After developing a simple scaling model based on these parameters, the model is compared with measured particle concentration profiles vs. particle numbers and field conditions. We then investigate extending this approach to superelliptical prisms by comparing experiments and model predictions for density metrics, field conditions, and particle numbers.

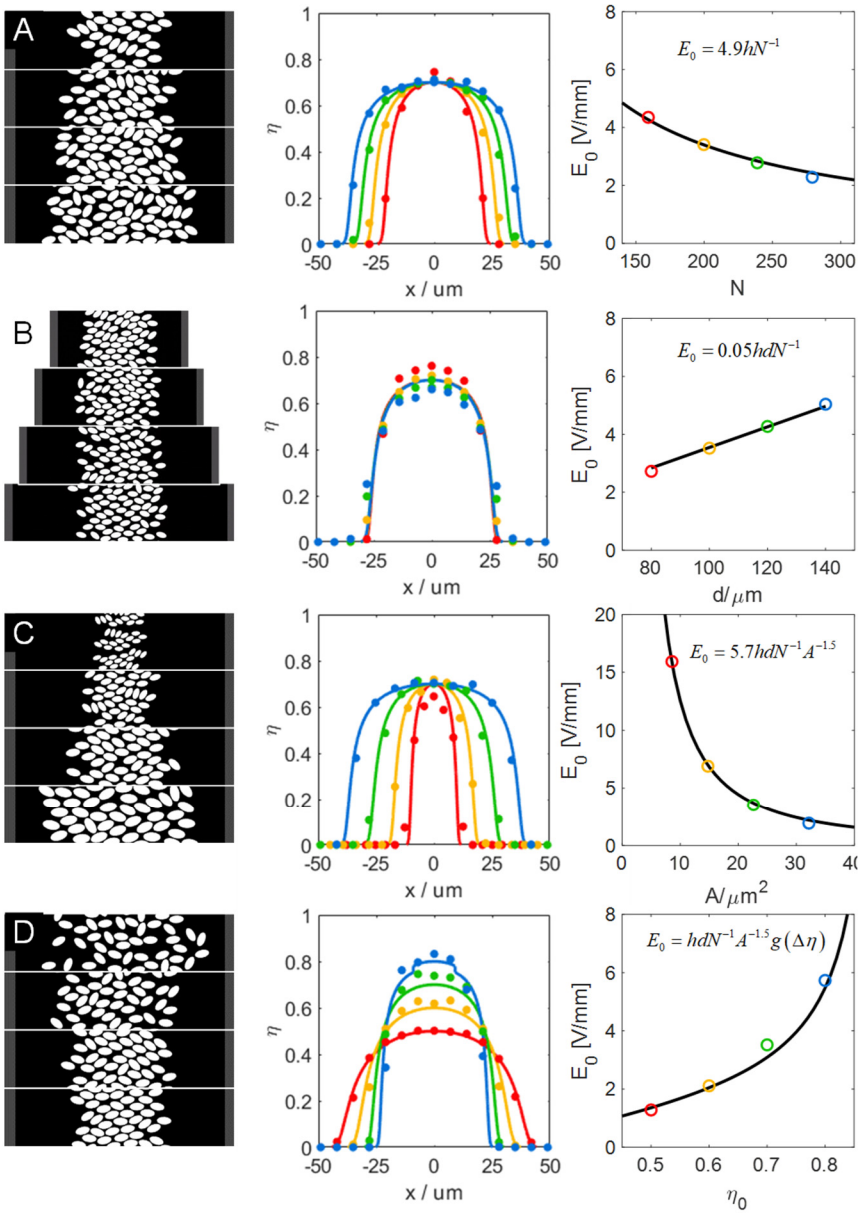


**Fig. 2. Comparing OFB model results to MC simulations to identify scaling for elliptical particle and field parameters.** (left) MC simulation renderings, (middle) density profiles from MC simulations (points) and OFB (line) (Eq. (3)), (right) trends in the applied electric field, $E_0$, vs. dependent variables with inset scaling relations (with all other variables fixed, see **Table 2**). Trends are shown for varying: (A) particle number in Eq. (4) at fixed central concentration, $\eta_0$, (B) electrode gap width, $d$, in Eq. (7), (C) particle area, $A$, in Eqs. (15), (16), and (D) central area fraction.

*Elliptical Prism Assemblies*

We start by computing density profiles for hard ellipse assemblies interacting with nonuniform AC electric fields via a dipole-field potential (Eq. (5)) from both the osmotic force balance, OFB (Eq. (3)), and Monte Carlo (MC) simulations. The potential in Eq. (5) was previously found to match microscopy experiments and MC simulations for disks, squares, ellipses, and rectangles in liquid, liquid crystal, and crystal states.[21] In addition, the equations of states used in the OFB (Eq. (3)) for varying aspect ratio hard ellipses in liquid, nematic, and crystal

states (Eqs. (10)-(12)) were recently validated in MC simulations,[32] but have not been tested against experiments. Practically, we simulated and modeled density profiles for a single aspect ratio ellipse using the parameters in **Tables 1,2** for (**Fig. 2**): (A) varying particle numbers, $N$, at a fixed central area fraction, $\eta_0$ (for the bin centered at $x$=0), (B) varying electrode gap, $d$, at fixed $N$ and $\eta_0$, (C), varying particle size at fixed aspect ratio, to vary particle area, $A_p$ (Eq. (15)) at fixed $\eta_0$, and (D) varying $\eta_0$ by adjusting the electric field, $E_0$, in Eq. (7) with all other variables fixed. For each case, **Fig. 2** includes renderings, density profiles from the OFB equation and MC simulations, and plots of the two variables that were adjusted with fit equations.

Several key findings are obtained from the results in **Fig. 2**. Overall good agreement is obtained between the OFB and MC density profiles for each of the conditions investigated, which allows analysis of how electric field, $E_0$, scales with each variable. For varying particle number at a fixed central area fractions in nematic states (Eq. (13)), **Fig. 2A** indicates the electric field scales with a $N^{-1}$ dependence (**Fig. 2A**) and linear dependence on box height, $h$, as given by Eq. (4). Building on this scaling, we next vary the electrode gap, $d$, width at a fixed number and central concentration (**Fig.2B**), which shows a simple linear scaling between $E_0$ and $d$, although the OFB and MC density profiles show small variations due to changing field shape (Eq. (7)). Varying particle size, at fixed aspect ratio and thickness, changes particle area (**Fig.2C**), and area fraction in the equations of state, but also particle volume in the dipole-field potential (Eq. (5)). The resulting field that is necessary to produce the same central density for different particle sizes, with all other parameters fixed, scales as $A_p^{-3/2}$. Understanding how particle area controls field mediated assembly provides an important foundation for analysis of additional superelliptical prism shaped particles (where different aspect ratios and corner features contribute to particle area).

**Table 1.** Global parameters for modeling dipole-field potentials in simulations and OFB.

| | | | | | |
|---|---|---|---|---|---|
| $\varepsilon_m/\varepsilon_0$[a] | 78 | $\omega$ (MHz) | 5 | $\psi$ (mV) | -15mV |
| $\varepsilon_p/\varepsilon_0$[b] | 3.2 | $d$ (μm)[f] | 100 | $B$ (kT) | 452 |
| $\sigma_m$ (μS/cm)[c] | 12.6 | $a_z$ (μm)[f] | 0.85 | $\kappa^{-1}$ (nm)[c] | 30 |
| $\sigma_p$ (μS/cm)[d] | 110 | $\alpha$ | 0.6 (n≥4) | $\delta$ (nm) | 100 |
| $f_{cm}$[e] | -0.37 | | | | |

[a]handbook values.[65] [b]manufacturer value. [c]conductivity meter, consistent with $CO_2$ saturated deionized $H_2O$ ionic strength. [d]prior study.[55] [e]calculated from Eq. (6).[f]electrode gap and particle thickness from laser scanning microscope.

**Table 2.** Parameters for MC simulations in specified figures.

| figure | shape | $a_x$ (μm) | $a_y$ (μm) | n | d (μm) | h (μm) | N | $\langle\rho\rangle$ (μm$^{-2}$) | $\eta_0$ |
|---|---|---|---|---|---|---|---|---|---|
| 2A | ellipse | 3.5 | 1.9 | 2 | 100 | 140 | 160-280 | 0.011-0.02 | 0.7 |
| 2B | ellipse | 3.5 | 1.9 | 2 | 80-140 | 140 | 200 | 0.01-0.18 | 0.7 |
| 2C | ellipse | 2.1-4.2 | 1.1-2.3 | 2 | 100 | 140 | 200 | 0.014 | 0.7 |
| 2D | ellipse | 3.5 | 1.9 | 2 | 100 | 140 | 200 | 0.014 | 0.5-0.8 |
| 4A | disk | 4 | 4 | 2 | 100 | 140 | 100 | 0.007 | 0.5-0.8 |
| 4B | square | 4 | 4 | 6 | 100 | 140 | 100 | 0.007 | 0.5-0.8 |
| 4C | rectangle | 4 | 2 | 4 | 100 | 140 | 180 | 0.013 | 0.5-0.8 |
| 5 | disk | 4 | 4 | 2 | 100 | 140 | 100 | 0.007 | 0.5~0.85 |
| 5 | ellipse | 4 | 2 | 2 | 100 | 140 | 200 | 0.014 | 0.5~0.85 |
| 5 | square | 4 | 4 | 6 | 100 | 140 | 100 | 0.007 | 0.5~0.9 |
| 5 | rectangle | 4 | 2 | 4 | 100 | 140 | 180 | 0.013 | 0.5~0.85 |

To understand the conditions necessary for liquid, liquid crystal, and crystal states assemble at different densities in nonuniform AC electric fields, we finally investigate how central density varies with field magnitude (**Fig.2D**). Density profiles are shown for central densities (and states) with $\eta_0$=0.5 (liquid), 0.6 (liquid), 0.7(nematic), and 0.8(crystal) (where states are related to

densities by Eq. (13))). Good agreement is obtained between MC simulations and the OFB, indicating the general validity of the equations of state, even for small numbers of particles in nonuniform density profiles varying on length scales comparable to particle dimensions. The scaling of the applied electric field with the central area fraction can be captured by a function of all variables investigated given by,

$$E_0 = hdN^{-1}A^{-1.5}g(\Delta\eta) = \langle\rho\rangle^{-1}A^{-1.5}g(\Delta\eta)$$
$$g(\Delta\eta) = -0.6\Delta\eta^{-1} + 9\Delta\eta + 3.7, \quad \Delta\eta = \eta_0 - \eta_{CP} \tag{20}$$

where $\langle\rho\rangle = N/(hd)$ is the average number density within the electrode gap and imaging region, and $\eta_{CP}$ is the close packed area fraction (*e.g.*, $\eta_{CP}$=0.907 for disks and ellipses). Referencing densities relative to their close packed state, when the crystal osmotic pressure diverges, is intended for subsequent analyses to consider different shaped particles with different close packed area fractions (*e.g.*, $\eta_{CP}$=1 for squares and rectangles).

It is important to note that the OFB model agrees with MC simulations that include dipole-dipole interactions (Eq. (19)). While the OFB model is based on equations of state for hard particles (or effective hard particles via Eq. (17)), the MC simulations have dipole-dipole interactions that are not accounted for in either the equations of state (Eqs. (10)-(12)) or the potential energy (Eq. (5)) in the OFB (Eq. (3)). However, the dipole-dipole interactions have a negligible effect for the states investigated in this work based on the good agreement in **Fig. 2**. This result is consistent with prior work for spherical particles in nonuniform AC electric fields with different morphologies and symmetries.[29-31] This behavior is generally understood as arising in nonuniform fields when the average dipole-dipole interaction is relatively negligible compared to dipole-field interactions in states with isotropically distributed dipoles, including crystal states,[11, 26-27, 66-67] as well as the dense liquid and liquid crystal states in this work. The relative balance of interactions also depends on field nonuniformity, where dipole-field interactions dominate in non-uniform fields (as in dielectrophoresis[11]) and dipole-dipole interactions are relatively more important in more uniform fields (as in electrorheological fluids[56-57, 68]).

*Model Predictions vs. Experiments: Elliptical Prisms*

To test the validity of the scaling captured by Eq. (20), we measure $N$, $\eta_0$, and $E_0$ in both MC simulations and optical microscopy experiments for elliptical prism particles between coplanar parallel electrodes (**Fig. 3**). Overall good agreement is observed between the OFB (lines) and the MC simulations (circles) for a broad range of conditions including liquid, nematic, and crystalline states. The greatest deviations are observed around $\eta_0 \approx 0.75$ where the continuous function, $g(\Delta\eta)$, is less well-suited to account for the discontinuous density change at the nematic-crystal transition ($\eta_F$=0.76, $\eta_M$=0.78 via Eq. (13)). Although a more complex form for $g(\Delta\eta)$ could be chosen to better match the model predictions and simulation data, a simple form was retained based on the precision needed to match with experimental results within their uncertainty (discussed in the following, including additional particle shapes). Results are only shown for $\eta_0$=0.5-0.87 since low density fluids are straightforward, and in experiments, higher density crystals approaching close packing can buckle into a three-dimensional system (as we have previously shown for spherical colloids[29, 31]).

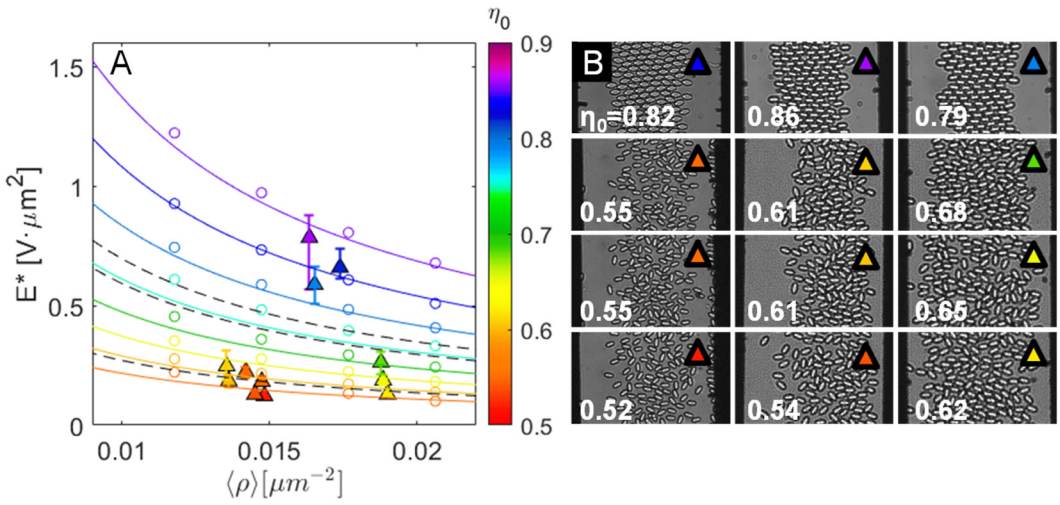


**Fig. 3. Comparing OFB model and optical microscopy experiments on elliptical prism particles to test $\langle\rho\rangle$, $\eta_0$, $E_0$ relationship.** (A) Plot of normalized field, $E^*=E_0A^{1.5}$, vs. average particle number density, $\langle\rho\rangle$, with (lines) constant density curves given by Eq. (20), (circles) OFB points from Eqs. (3),(4), and (triangles) optical microscopy measurements of time-averaged density photolithographic epoxy particles for parameters and error bars in **Table 3**. Dashed lines indicate nematic, freezing, and melting (from bottom to top) transitions from Eq. (13). (B) Microscopy images of particle configurations corresponding to each point in panel A as indicated by colored symbol with central area fraction indicated. Density increases from left to right from liquid to nematic to crystal states. The electrode gap, d=100 μm, and the particle sizes listed in Table 3 provide internal scale bars for each image.

**Table 3.** Parameters for optical microscopy experiments in specified figures.

| Fig. | shape | $a_x$ (μm)[a] | $a_y$ (μm)[a] | n[a] | h (μm)[b] | N[c] | $\langle\rho\rangle$ (μm$^{-2}$)[d] | $\eta_0$ | $\eta_H$, $\eta_L$ | $E_0$(V/mm) |
|---|---|---|---|---|---|---|---|---|---|---|
| 3B1 | ellipse | 3.35 | 1.7 | 2 | 114 | 164 | 0.014 | 0.52 | 0.52-0.52 | 1.4 |
| 3B2 | ellipse | 3.35 | 1.7 | 2 | 114 | 163 | 0.014 | 0.55 | 0.55-0.57 | 2.1 |
| 3B3 | ellipse | 3.35 | 1.7 | 2 | 114 | 157 | 0.014 | 0.55 | 0.52-0.57 | 2.6 |
| 3B4 | ellipse | 3.4 | 1.8 | 2 | 140 | 197 | 0.014 | 0.54 | 0.53-0.55 | 1.3 |
| 3B5 | ellipse | 3.4 | 1.8 | 2 | 140 | 185 | 0.013 | 0.61 | 0.58-0.62 | 1.9 |
| 3B6 | ellipse | 3.4 | 1.8 | 2 | 140 | 184 | 0.013 | 0.61 | 0.55-0.66 | 2.6 |
| 3B7 | ellipse | 3.5 | 1.9 | 2 | 140 | 258 | 0.018 | 0.62 | 0.61-0.63 | 1.2 |
| 3B8 | ellipse | 3.5 | 1.9 | 2 | 140 | 256 | 0.018 | 0.65 | 0.63-0.67 | 1.7 |
| 3B9 | ellipse | 3.5 | 1.9 | 2 | 140 | 255 | 0.018 | 0.68 | 0.63-0.72 | 2.4 |
| 3B10 | ellipse | 3.5 | 1.9 | 2 | 58 | 92 | 0.016 | 0.86 | 0.84-0.87 | 7.3 |
| 3B11 | ellipse | 3.6 | 2.1 | 2 | 46 | 69 | 0.015 | 0.84 | 0.79-0.87 | 7.3 |
| 3B12 | ellipse | 3.5 | 1.9 | 2 | 58 | 93 | 0.016 | 0.79 | 0.76-0.81 | 5.4 |
| 6B1 | disk | 3.9 | 3.9 | 2 | 112 | 130 | 0.012 | 0.86 | 0.85-0.86 | 3.6 |
| 6B2 | disk | 4 | 4 | 2 | 140 | 141 | 0.010 | 0.78 | 0.76-0.82 | 1.4 |
| 6B3 | disk | 3.9 | 3.9 | 2 | 112 | 74 | 0.007 | 0.46 | 0.44-0.47 | 0.4 |
| 6B4 | square | 3.4 | 3.4 | 6 | 140 | 152 | 0.011 | 0.87 | 0.79-0.92 | 2.5 |
| 6B5 | square | 3.4 | 3.4 | 6 | 140 | 183 | 0.013 | 0.77 | 0.74-0.79 | 0.9 |
| 6B6 | square | 3.4 | 3.4 | 6 | 140 | 123 | 0.009 | 0.56 | 0.54-0.57 | 0.4 |
| 6B7 | rectangle | 4 | 2 | 4 | 85 | 116 | 0.014 | 0.81 | 0.79-0.82 | 3.3 |
| 6B8 | rectangle | 4 | 2 | 4 | 140 | 202 | 0.014 | 0.70 | 0.66-0.70 | 1.4 |
| 6B9 | rectangle | 4 | 2 | 4 | 140 | 202 | 0.014 | 0.62 | 0.61-0.63 | 0.7 |

[a]laser scanning microscope (error ±0.1μm). [b]image analysis (error ±pixel size), [c]time average based on fluctuations at imaging window edge. [d]based on *d*=100 μm as given in Table 1.

We next compare optical microscopy experiments with elliptical prism particles (**Fig. 3B**) with the OFB model predictions in Eq. (20). Because the potentials used in the MC simulations

were obtained from inverse Boltzmann[49-50] and inverse MC[55] analyses of experiments on identical particle materials and similar shapes, the experimentally measured scaling of $N$, $\eta_0$, and $E_0$ are also expected to agree with the MC and OFB results in **Fig. 3A**. Specific experimental details of the particle and field characteristics are reported in **Tables 1-3**. Practically, particles were measured for different $N$, $\eta_0$, and $E_0$ corresponding to liquid, liquid crystal, and crystal states (using methods described in detail in prior work[21]).

The agreement between the microcopy measurements, simulations, and the OFB scaling are good in terms of capturing the observed system state and central concentration at each condition. Discrepancies between experiments and the model are observed primarily for experimental conditions that are perhaps less satisfactory in terms of meeting the assumptions in the OFB model. For example, particles approaching the electrode edge encounter strong field gradients that may influence the validity of the local density approximation, and crystals with vacancies, misoriented particles, grain boundaries and other defects can significantly influence density profiles for the very small system sizes probed in the measurements. Despite these possible limitations based on practical experimental considerations, overall, the model performs well for predicting the system density and states for given particle numbers and field strengths.

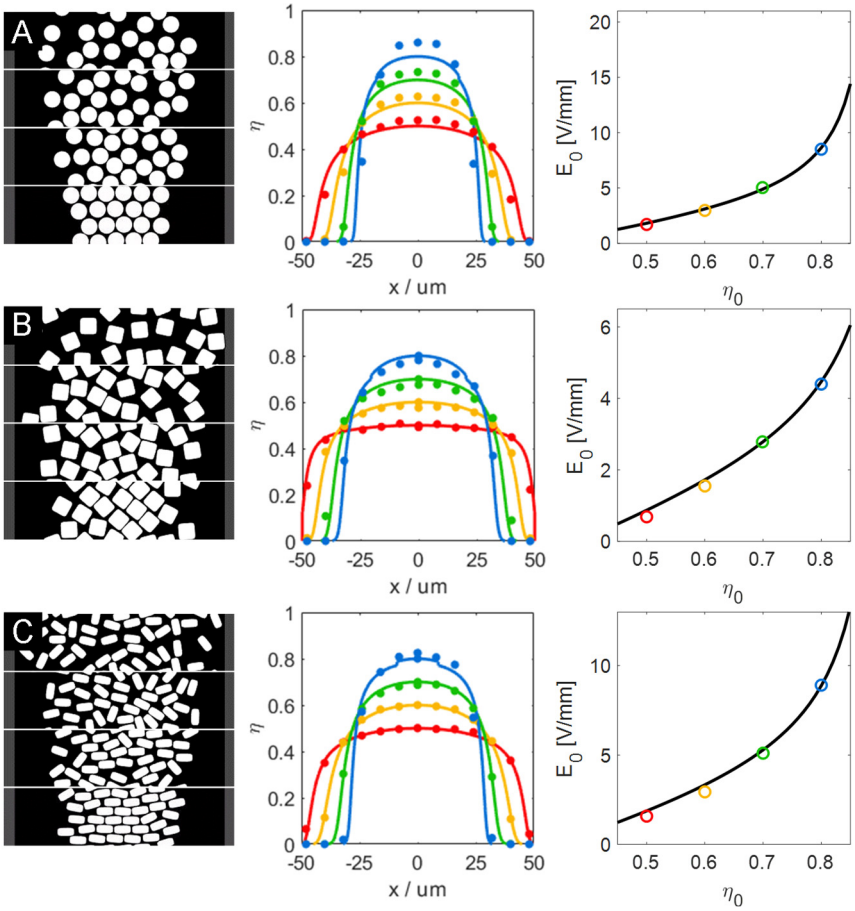


**Fig. 4. Comparing OFB model results to MC simulations to identify scaling for disks, squares, and rectangles (superelliptical) particles and field parameters.** (left) MC simulation renderings, (middle) density profiles from MC simulations (points) and OFB (line) (Eq. (3)), (right) trends in the applied electric field, $E_0$, vs. central density (with all other variables fixed, see **Table 2**). Trends are shown for varying central density of: (A) disks, (B) squares, and (C) rectangles. Lines in right panels are given by Eq. (20).

*Extension to Additional Anisotropic Particle Shapes*

Given the success of the OFB model in Eq. (20) for capturing experimental systems of quasi-2D elliptical prism particles, we next explore the suitability of the model for quasi-2D assembly of other particle shapes in nonuniform AC electric fields. Practically, we investigate the scaling of density profiles and field parameters in MC simulations and the OFB model for disk, square, and rectangular prism particles (**Fig. 4**), which we can also fabricate as in prior experimental microscopy studies.[21] To aid comparison and contrast of different shapes, we fix each particles largest axis to the same dimension in all cases (*i.e.*, $a_x$=4μm) and then adjust aspect ratio via the smaller axis dimension ($a_y$) and introduce corners via $n$ in Eq. (14). MC simulations of each particle shape at different central densities and electric field amplitudes (**Fig. 4**), which also have different particle numbers and areas, show Eq. (20) is also effective at capturing the scaling of relevant variables similar to trends for ellipses (**Fig. 2**). The predicted density profiles from the OFB (Eq. (3)) quantitively capture the MC simulation density profiles for each shape using the equations of state in Eqs. (8)-(12) (with $\alpha$=0.6 for squares and rectangles in Eq. (10)). The OFB and MC density profiles are also in good agreement for all liquid, liquid crystal, and crystal states. The greatest discrepancy is observed for the high density crystalline disk state (**Fig. 4A**) that approaches an exceptionally small system size with large density variations comparable to particle dimensions. These results demonstrate the accuracy of the model in Eq. (20) and the equations of state for quasi-2D liquid, nematic, and crystal states of circular, elliptical, square, and rectangular prism particles in nonuniform AC electric fields.

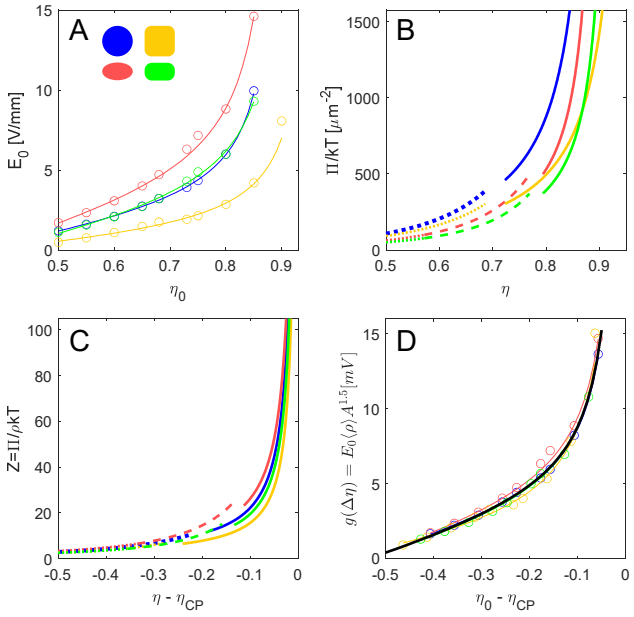


**Fig. 5. Understanding concentration dependent electric field magnitude by comparing equations of state for particle shapes.** (A) Electric field vs. central area fraction for the particle shapes in Fig . 4 from (circles) OFB model predictions and (lines) Eq. (20) using individually fit functions for g(Δη) (see **Table 2** for details). (B) Osmotic pressure vs. concentration for four particle shapes for: (dotted) fluid (Eq. (10)), (dashed) nematic (Eq. (11)), and (solid) crystal (Eq. (12)) with transition given by Eq. (13). (C) Compressibility factors, Z, for four particle shapes vs. concentration relative to close packed crystal state, $\Delta\eta=\eta-\eta_{CP}$. (D) Re-scaling electric field with scaling from **Fig. 2** vs. $\Delta\eta=\eta_0-\eta_{CP}$ for four particle shapes to give g(Δη) in Eq. (20) (black line).

To understand how the functional form for $g(\Delta\eta)$ in Eq. (20) was designed to capture the scaling of relevant parameters for all shapes in **Figs. 2-4**, a number of unscaled and re-scaled quantities are reported to demonstrate the relevant factors for consideration (**Fig. 5**). Plotting the unscaled values for $E_0$ vs. $\eta_0$ from the OFB produces unique trends for each particle shape (**Fig. 5A**) without any obvious trends dependent on particle shape metrics (*e.g.*, anisotropy, corners, area, etc.). likewise, the equations of state for each particle shape for all states and concentrations (**Fig. 5B**) show different intercepts, gradients, transitions, and a different order from the trends in the unscaled $E_0$ vs. $\eta_0$ data (**Fig. 5A**).

Because the particles are different sizes in **Figs. 2-4**, and therefore have different local number densities, $\rho$, for the same local area fraction, the compressibility factor is plotted (**Fig. 5C**) to focus on area fraction without the $\rho kT$ prefactor in Eq. (8). In addition, area fractions referenced to the close packed crystal area fraction aligns the osmotic pressure divergence for each particle shape. The disk and ellipses have the same close packed limit ($\eta_{CP}$=0.907) and squares and rectangles have the same limits for the same value of $n$ in Eq. (14) ($\eta_{CP}\rightarrow 1$ as $n\rightarrow\infty$). This rescaling acts as a sort of reference to corresponding states (*e.g.*, compare with 3D polyhedral liquids[36]), which collapses the compressibility factors for low density liquid and high density crystal states for all particle shapes. Because the OFB is based on integrating Z, and because different particle sizes produce different particle numbers and areas, rescaling the $E_0$ vs. $\eta_0$ data (**Fig. 5A**) as $E_0/A^{1.5}\langle\rho\rangle$ vs. $\Delta\eta$ (**Fig. 5D**) collapses the data onto a single trend. While the collapse is imperfect with minor residual systematic variations in the vicinity of the transition regions, the deviations relative to individual $g(\Delta\eta)$ data sets are within the uncertainty in the equations of states (and experimental uncertainty in microscopy measurements in this work). As such, the small deviations are not significant when comparing Eq. (20) to the MC simulation results in **Fig. 4**.

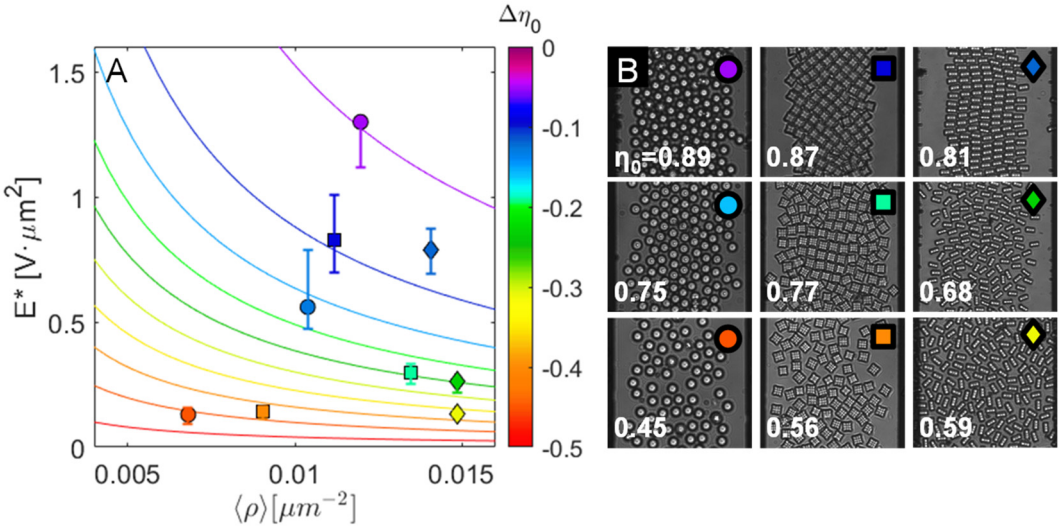


**Fig. 6. Comparing OFB model and optical microscopy experiments on circular, square, and rectangular (superelliptical) prism particles to test $\langle\rho\rangle$, $\eta_0$, $E_0$ relationship.** (A) Plot of normalized field, $E^*=E_0A^{1.5}$, vs. average particle number density, $\langle\rho\rangle$, with (lines) constant density curves given by Eq. (20) and (points) optical microscopy measurements of time-averaged density photolithographic epoxy particles for parameters and error bars in **Table 3**. (B) Microscopy images of particle configurations corresponding to each point in panel A as indicated by colored symbol with central area fraction indicated. Density increases from liquid to nematic to crystal states. The electrode gap, d=100 μm, and the particle sizes listed in **Table 3** provide internal scale bars for each image.

*Model Predictions vs. Experiments: Superelliptical Prisms*

As in the test of the OFB model against optical microscopy experiments on elliptical prisms particles (**Fig. 3**), we now investigate the validity of the scaling in Eq. (20) for modeling $N$, $\eta_0$, and $E_0$ in quasi-2D systems of superelliptical prism particles including disks, squares, and rectangles (**Fig. 6**). Results in **Fig. 6** directly compare the OFB predictions against optical microscopy data for different concentrations of each particle shape representing predominantly liquid, liquid crystal, and crystal states between coplanar parallel electrodes (**Fig. 3**). We don't compare again with MC simulations given that they are already used to validate the OFB model for different shaped particles in **Figs. 4, 5**, and the potential in Eq. (5) was already validated via inverse analyses of similar experiments.[49] As in all comparisons of the OFB prediction with simulations and experiments thus far, the agreement is good overall within the uncertainty in the equations of state, statistical uncertainty in the microscopy experiments, and experimental parameter uncertainty (see **Tables 1-3**). The overall good agreement between the OFB model, MC simulations, and experiments shows the generality of the model in Eq. (20) and equations of state for different particle shapes, sizes, numbers, and states in nonuniform AC electric fields.

## Conclusions

We developed a model to predict the electric field strength to assemble different shaped particles into quasi-2D fluid, nematic, and crystal states with known densities. The model was derived by balancing the quasi-2D osmotic pressure of different shaped particles within different states against the force due to a nonuniform AC electric field compressing particles at the electric field minimum (due to an induced dipole-field potential). The model includes new simple equations of state for all superelliptical shapes within liquid, nematic, and crystal states, which accurately capture multistate density profiles from MC simulations. By comparing the applied electric field and central density within states in the model and MC simulations, we demonstrate the model accurately predicts the central density and state for different particle shapes sizes, electrode gap dimensions, and system sizes. After demonstrating agreement between the model and MC simulations, the model is compared against optical microscopy experiments on quasi-2D assemblies of micron sized circular, elliptical, square, and rectangular prism particles, and is shown to accurately capture liquid, liquid crystal, and crystal states and densities within the limits of experimental uncertainty. In short, the osmotic force balance model provides accurate predictions of electric field magnitudes to obtain specific microstructures of different particle shapes in quasi-2D systems. The ability of the model to predict equilibrium liquid, liquid crystal, and crystal states of different shaped particles in AC electric fields provides a basis to further develop models that capture non-equilibrium dynamics and control of transient assembly processes between different states using electric field mediated assembly mechanisms.

## Conflicts of interest

There are no conflicts to declare.

## Acknowledgments

We acknowledge financial support by the National Science Foundation CBET 2113594.

# References


1. Damasceno, P. F.; Engel, M.; Glotzer, S. C. Predictive Self-Assembly of Polyhedra into Complex Structures. *Science* **2012,** *337*, 453-457.
2. Torres-Díaz, I.; Hendley, R. S.; Mishra, A.; Yeh, A. J.; Bevan, M. A. Hard Superellipse Phases: Particle Shape Anisotropy & Curvature. *Soft Matter* **2022,** *18*, 1319-1330.
3. Perrin, J. B. Mouvement Brownien Et Realite Moleculaire. *Ann. Chim. Phys.* **1909,** *18*, 5-118.
4. Davis, K. E.; Russel, W. B.; Glantschnig, W. J. Disorder-to-Order Transition in Settling Suspensions of Colloidal Silica: X-Ray Measurements. *Science* **1989,** *245*, 507-510.
5. Beek, D. v. d.; Schilling, T.; Lekkerkerker, H. N. W. Gravity-Induced Liquid Crystal Phase Transitions of Colloidal Platelets. *J. Chem. Phys.* **2004,** *121*, 5423-5426.
6. Eckert, T.; Schmidt, M.; de las Heras, D. Gravity-Induced Phase Phenomena in Plate-Rod Colloidal Mixtures. *Communications Physics* **2021,** *4*, 202.
7. Beckham, R. E.; Bevan, M. A. Interfacial Colloidal Sedimentation Equilibrium I. Intensity Based Confocal Microscopy. *J. Chem. Phys.* **2007,** *127*, 164708.
8. Lu, M.; Bevan, M. A.; Ford, D. M. Interfacial Colloidal Sedimentation Equilibrium. Ii. Closure-Based Density Functional Theory. *The Journal of Chemical Physics* **2007,** *127*.
9. Schmidt, M.; Dijkstra, M.; Hansen, J.-P. Competition between Sedimentation and Phase Coexistence of Colloidal Dispersions under Gravity. *J. Phys.: Condens. Matter* **2004,** *16*, S4185–S4194.
10. Savenko, S. V.; Dijkstra, M. Sedimentation and Multiphase Equalibria in Suspensions of Colloidal Hard Rods. *Physical Review E* **2004,** *70*, 051401-1 - 051401-7.
11. Pohl, H. A. *Dielectrophoresis : The Behavior of Neutral Matter in Nonuniform Electric Fields*. Cambridge University Press: Cambridge, **1978**; p 590.
12. Russel, W. B.; Saville, D. A.; Schowalter, W. R. *Colloidal Dispersions*. Cambridge University Press: New York, **1989**.
13. Morgan, H.; Green, N. G. *Ac Electrokinetics: Colloids and Nanoparticles*. Research Studies Press: Philadelphia, PA, **2003**.
14. Pethig, R. *Dielectrophoresis: Theory, Methodology, and Biological Applications*. John Wiley & Sons, Incorporated: **2017**.
15. Lumsdon, S. O.; Kaler, E. W.; Velev, O. D. Two-Dimensional Crystallization of Microspheres by a Coplanar Ac Electric Field. *Langmuir* **2004,** *20*, 2108-2116.
16. Bahukudumbi, P.; Everett, W. N.; Beskok, A.; Huff, G. H.; Lagoudas, D.; Ounaies, Z.; Bevan, M. A. Colloidal Microstructures, Transport, and Impedance Properties within Interfacial Microelectrodes. *Appl. Phys. Lett.* **2007,** *90*, 224102.
17. Singh, J. P.; Lele, P. P.; Nettesheim, F.; Wagner, N. J.; Furst, E. M. One- and Two-Dimensional Assembly of Colloidal Ellipsoids in Ac Electric Fields. *Physical Review E* **2009,** *79*, 050401.
18. Shah, A. A.; Kang, H.; Kohlstedt, K. L.; Ahn, K. H.; Glotzer, S. C.; Monroe, C. W.; Solomon, M. J. Liquid Crystal Order in Colloidal Suspensions of Spheroidal Particles by Direct Current Electric Field Assembly. *Small* **2012,** *8*, 1551-1562.
19. Kuijk, A.; Troppenz, T.; Filion, L.; Imhof, A.; van Roij, R.; Dijkstra, M.; van Blaaderen, A. Effect of External Electric Fields on the Phase Behavior of Colloidal Silica Rods. *Soft Matter* **2014,** *10*, 6249-6255.
20. Stelson, A. C.; Penterman, S. J.; Liddell Watson, C. M. Electric Field-Directed Assembly of Fullerene Crystal Rods into Hierarchical Films. *Journal of Materials Chemistry C* **2018,** *6*, 11118-11127.
21. Hendley, R. S.; Zhang, L.; Bevan, M. A. Design Rules for 2d Field Mediated Assembly of Different Shaped Colloids into Diverse Microstructures. *Soft Matter* **2022,** *18*, 9273-9282.
22. Dozov, I.; Paineau, E.; Davidson, P.; Antonova, K.; Baravian, C.; Bihannic, I.; Michot, L. J. Electric-Field-Induced Perfect Anti-Nematic Order in Isotropic Aqueous Suspensions of a Natural Beidellite Clay. *J Phys Chem B* **2011,** *115*, 7751-65.
23. Herlihy, K. P.; Nunes, J.; DeSimone, J. M. Electrically Driven Alignment and Crystallization of Unique Anisotropic Polymer Particles. *Langmuir* **2008,** *24*, 8421-8426.

24. Yanai, N.; Sindoro, M.; Yan, J.; Granick, S. Electric Field-Induced Assembly of Monodisperse Polyhedral Metal–Organic Framework Crystals. *Journal of the American Chemical Society* **2013,** *135*, 34-37.
25. Shields Iv, C. W.; Zhu, S.; Yang, Y.; Bharti, B.; Liu, J.; Yellen, B. B.; Velev, O. D.; Lopez, G. P. Field-Directed Assembly of Patchy Anisotropic Microparticles with Defined Shape. *Soft Matter* **2013,** *9*, 9219-9229.
26. Sullivan, M. T.; Zhao, K.; Hollingsworth, A. D.; Austin, R. H.; Russel, W. B.; Chaikin, P. M. An Electric Bottle for Colloids. *Phys. Rev. Lett.* **2006,** *96*, 015703.
27. Leunissen, M. E.; Sullivan, M. T.; Chaikin, P. M.; van Blaaderen, A. Concentrating Colloids with Electric Field Gradients. I. Particle Transport and Growth Mechanism of Hard-Sphere-Like Crystals in an Electric Bottle. *J. Chem. Phys.* **2008,** *128*, 164508-11.
28. Hwang, H.; Weitz, D. A.; Spaepen, F. Direct Observation of Crystallization and Melting with Colloids. *Proceedings of the National Academy of Sciences* **2019,** *116*, 1180-1184.
29. Edwards, T. D.; Beltran-Villegas, D. J.; Bevan, M. A. Size Dependent Thermodynamics and Kinetics in Electric Field Mediated Colloidal Crystal Assembly. *Soft Matter* **2013,** *9*, 9208-9218.
30. Zhang, J.; Zhang, Y.; Bevan, M. A. Spatially Varying Colloidal Phase Behavior on Multi-Dimensional Energy Landscapes. *J. Chem. Phys.* **2020,** *152*, 054905.
31. Juarez, J. J.; Feicht, S. E.; Bevan, M. A. Electric Field Mediated Assembly of Three Dimensional Equilibrium Colloidal Crystals. *Soft Matter* **2012,** *8*, 94-103.
32. Baron, P. B.; Hendley, R. S.; Bevan, M. A. Anisotropic Particle Multiphase Equilibria in Nonuniform Fields. *The Journal of Chemical Physics* **2023,** *159*.
33. Kraft, A.; Klapp, S. H. L. Freezing of a Soft-Core Fluid in a One-Dimensional Potential: Predictions Based on a Pressure-Balance Equation. *Physical Review E* **2020,** *101*, 012609.
34. Carnahan, N. F.; Starling, K. E. Equation of State for Nonattracting Rigid Spheres. *J. Chem. Phys.* **1969,** *51*, 635.
35. Hall, K. R. Another Hard-Sphere Equation of State. *J. Chem. Phys.* **1972,** *57*, 2252-2254.
36. Vo, T.; Glotzer, S. C. Principle of Corresponding States for Hard Polyhedron Fluids. *Molecular Physics* **2019,** *117*, 3518-3526.
37. Santos, A.; López de Haro, M.; Bravo Yuste, S. An Accurate and Simple Equation of State for Hard Disks. *The Journal of Chemical Physics* **1995,** *103*, 4622-4625.
38. Cuesta, J. A.; Tejero, C. F.; Baus, M. Isotropic-Nematic Transition of Hard Ellipses. *Physical Review A* **1989,** *39*, 6498-6506.
39. Cuesta, J. A.; Frenkel, D. Monte Carlo Simulation of Two-Dimensional Hard Ellipses. *Phys Rev A* **1990,** *42*, 2126-2136.
40. Xu, W.-S.; Li, Y.-W.; Sun, Z.-Y.; An, L.-J. Hard Ellipses: Equation of State, Structure, and Self-Diffusion. *The Journal of chemical physics* **2013,** *139*, 024501.
41. Bautista-Carbajal, G.; Odriozola, G. Phase Diagram of Two-Dimensional Hard Ellipses. *The Journal of Chemical Physics* **2014,** *140*, 204502.
42. Boublík, T. Equation of State of Hard Disk and 2d Convex Bodies. *Molecular Physics* **2011,** *109*, 1575-1580.
43. Piazza, R.; Bellini, T.; Degiorgio, V. Equilibrium Sedimentation Profiles of Screened Charged Colloids: A Test of the Hard-Sphere Equation of State. *Physical Review Letters* **1993,** *71*, 4267-4270.
44. Rutgers, M. A.; Dunsmuir, J. H.; Xue, J.-Z.; Russel, W. B.; Chaikin, P. M. Measurement of the Hard-Sphere Equation of State Using Screened Charged Polystyrene Colloids. *Phys. Rev. B* **1996,** *53*, 5043-5046.
45. Beltran-Villegas, D. J.; Schultz, B. A.; Nguyen, N. H. P.; Glotzer, S. C.; Larson, R. G. Phase Behavior of Janus Colloids Determined by Sedimentation Equilibrium. *Soft Matter* **2014,** *10*, 4593-4602.
46. Ginot, F.; Solon, A.; Kafri, Y.; Ybert, C.; Tailleur, J.; Cottin-Bizonne, C. Sedimentation of Self-Propelled Janus Colloids: Polarization and Pressure. *New Journal of Physics* **2018,** *20*, 115001.
47. Gillespie, C.; Milner, S. T. Using Osmotic Pressure Simulations to Test Potentials for Ions. *Soft Matter* **2020,** *16*, 9816-9821.

48. Hosseni, A.; Ashbaugh, H. S. Osmotic Force Balance Evaluation of Aqueous Electrolyte Osmotic Pressures and Chemical Potentials. *Journal of Chemical Theory and Computation* **2023,** *19*, 8826-8838.
49. Zhang, L.; Pellicciotti, A. J.; Hendley, R. S.; Wang, X.; Bevan, M. A. Simple Models of Directly Measured Energy Landscapes for Different Shaped Particles in Nonuniform Ac Electric Fields. *Langmuir* **2024,** accepted.
50. Rupp, B.; Torres-Diaz, I.; Hua, X.; Bevan, M. A. Measurement of Anisotropic Particle Interactions with Nonuniform Ac Electric Fields. *Langmuir* **2018,** *34*, 2497-2504.
51. Avendaño, C.; Escobedo, F. A. Phase Behavior of Rounded Hard-Squares. *Soft Matter* **2012,** *8*, 4675.
52. Hansen, J. P.; McDonald, I. R. *Theory of Simple Liquids*. Academic Press: London, **1986**.
53. Torres-Díaz, I.; Rupp, B.; Yang, Y.; Bevan, M. A. Energy Landscapes for Ellipsoids in Non-Uniform Ac Electric Fields. *Soft Matter* **2018,** *14*, 934-944.
54. Juarez, J. J.; Liu, B. G.; Cui, J.-Q.; Bevan, M. A. Kt-Scale Colloidal Interactions in High-Frequency Inhomogeneous Ac Electric Fields. Ii. Concentrated Ensembles. *Langmuir* **2011,** *27*, 9219-9226.
55. Hendley, R. S.; Torres-Díaz, I.; Bevan, M. A. Anisotropic Colloidal Interactions & Assembly in Ac Electric Fields. *Soft Matter* **2021,** *17*, 9066-9077.
56. Adriani, P. M.; Gast, A. P. A Microscopic Model of Electrorheology. *Phys. Fluids* **1988,** *31*, 2757-2768.
57. Tao, R.; Sun, J. M. Three-Dimensional Structure of Induced Electrorheological Solid. *Phys. Rev. Lett.* **1991,** *67*, 398.
58. Morgan, H.; García Izquierdo, A.; Bakewell, D.; Green, N. G.; Ramos, A. The Dielectrophoretic and Travelling Wave Forces Generated by Interdigitated Electrode Arrays: Analytical Solution Using Fourier Series. *Journal of Physics D: Applied Physics* **2001,** *34*, 1553-1561.
59. Stillinger, F. H.; Salsburg, Z. W. Limiting Polytope Geometry for Rigid Rods, Disks, and Spheres. *Journal of Statistical Physics* **1969,** *1*, 179-225.
60. Donev, A.; Burton, J.; Stillinger, F. H.; Torquato, S. Tetratic Order in the Phase Behavior of a Hard-Rectangle System. *Physical Review B* **2006,** *73*, 054109.
61. Engel, M.; Anderson, J. A.; Glotzer, S. C.; Isobe, M.; Bernard, E. P.; Krauth, W. Hard-Disk Equation of State: First-Order Liquid-Hexatic Transition in Two Dimensions with Three Simulation Methods. *Physical Review E* **2013,** *87*, 042134.
62. Regnaut, C.; Ravey, J. C. Application of the Adhesive Sphere Model to the Structure of Colloidal Suspensions. *J. Chem. Phys.* **1989,** *91*, 1211-1221.
63. Barker, J. A.; Henderson, D. Perturbation Theory and Equation of State for Fluids. Ii. A Successful Theory of Liquids. *J. Chem. Phys.* **1967,** *47*, 4714-4721.
64. Hernandez, C. J.; Mason, T. G. Colloidal Alphabet Soup: Monodisperse Dispersions of Shape-Designed Lithoparticles. *The Journal of Physical Chemistry C* **2007,** *111*, 4477-4480.
65. Lide, D. R. *Crc Handbook of Chemistry and Physics*. CRC Press: New York, **2000**; Vol. 80.
66. Wang, X. B.; Huang, Y.; Burt, J. P. H.; Markx, G. H.; Pethig, R. Selective Dielectrophoretic Confinement of Bioparticles in Potential-Energy Wells. *J. Phys. D: Appl. Phys.* **1993,** *26*, 1278-1285.
67. Khusid, B.; Acrivos, A. Effects of Interparticle Electric Interactions on Dielectrophoresis in Colloidal Suspensions. *Phys. Rev. E* **1996,** *54*, 5428.
68. Gast, A. P.; Zukoski, C. F. Electrorheological Fluids as Colloidal Suspensions. *Adv. Colloid Interface Sci.* **1989,** *30*, 153-202.

## For Table of Contents Use Only

(8.0139 in. wide x 6.2739 in high, approx. 5:4)